# Microstructure and magnetism of nanoparticles with $\gamma$-Fe core surrounded by $\alpha$-Fe and iron oxide shells

Maria Paz Fernández-García,[*] Pedro Gorria,[†] and Jesús A. Blanco[‡]
*Departamento de Física, Universidad de Oviedo, Calvo Sotelo, s/n, 33007 Oviedo, Spain*

Antonio B. Fuertes and Marta Sevilla
*Instituto Nacional del Carbón, CSIC, Apartado 73, 33080 Oviedo, Spain*

Roberto Boada and Jesús Chaboy
*Instituto de Ciencia de los Materiales de Aragón and Depto. de Física de la Materia Condensada, CSIC–Universidad de Zaragoza, 50009 Zaragoza, Spain*

David Schmool
*IN-IFIMUP and Depto. de Física, Universidade do Porto, Rua do Campo Alegre, 687, 4169-007 Porto, Portugal*

Jean-Marc Grenèche
*LPEC, UMR CNRS 6087, Université du Maine, 72085 Le Mans Cedex 9, France*

Iron-carbon nanocomposites have been elaborated by means of a simple chemical procedure based on *in situ* synthesis of iron nanoparticles within the nanopores of an activated carbon. The Fe nanoparticles present a broad particle-size distribution (5–40 nm). A combined structural and magnetic study seems to suggest that most of the nanoparticles of mean size $\sim$15 nm have exotic "onionlike" core-shell morphology of $\gamma$-Fe nucleus surrounded by a concentric double shell of $\alpha$-Fe and maghemitelike oxide. The true nature of Fe-oxide was successfully evidenced through room temperature x-ray absorption spectroscopy. The whole system does not reach a fully superparamagnetic regime even at 750 K, probably due to higher blocking temperatures for the largest nanoparticles. Mössbauer spectrometry indicates that low temperature para-to-antiferromagnetic transition for the $\gamma$-Fe phase cannot be discarded. In addition, the external Fe-oxide shell exhibits spin-glass behavior giving rise to the freezing of its magnetic moments at low temperatures. Hence, we propose a competing double magnetic coupling: (i) the oxide shell/$\alpha$-Fe interaction and (ii) the possible antiferromagnetic coupling between $\gamma$-Fe nucleus and $\alpha$-Fe layer; as being both responsible for the observed exchange bias effect at $T=5$ K ($H_{ex} \approx 150$ Oe).

## I. INTRODUCTION

The large variety of magnetic scenarios displayed by nanoparticle (NP) systems is mainly governed by the reduced size and/or miscellaneous morphologies of the particles because surface, interface, or finite-size effects play an important role.[1–5] Furthermore, the physical-chemical nature of the surrounding medium or matrix (amorphous or crystalline, insulating or conducting, magnetic or nonmagnetic, etc.) strongly influences the magnetic properties of the NPs.[6–13] The complete understanding of the correlation between microstructure, morphology, and magnetic behavior is, at present, an interesting and novel issue that can lead to functionalize NPs for potential applications.[14–16]

In the particular case of Fe nanoparticulate systems, the essential problem is that they commonly burn up when they are put into contact with air due to the strong and fast reactivity of Fe. To avoid such a situation, encapsulating Fe-NPs through the passivation with a Fe-oxide layer both protects and stabilizes the formation of Fe-NPs. Consequently, the NPs present core-shell morphology.[17–25] In this situation, strong exchange magnetic coupling between the iron particle core and the iron oxide shell gives rise to modifications in the coercivity, the magnetic anisotropy, and to the appearance of an exchange-bias (EB) effect.[26–35] This phenomenology is mostly observed in thin films composed of alternating ferromagnetic/antiferromagnetic (FM/AFM) layers when the Néel temperature ($T_N$) of the AFM layer is smaller than the Curie temperature ($T_C$) of the FM one. In order to minimize the exchange energy at the interface, the magnetic moments of both FM and AFM layers become coupled, thus giving rise to an effective uniaxial anisotropy. Recently, EB has been reported below 50 K for iron nanostructured granular systems coated by a thin ferrimagnetic (FIM) iron oxide layer. The existence of such FIM shell around Fe-NPs is responsible for the shifting of the hysteresis loops at temperatures much lower than the $T_N$ of the iron oxides as the sample is cooled under an applied magnetic field. It seems to be a general agreement that the existence of unidirectional exchange anisotropy created by the "freezing state" of the Fe-oxide magnetic moments is responsible of the EB below 50 K.[22,25,36,37] However, this EB may be altered when other magnetic phases are present. Consequently, the possibility of manufacturing Fe-NPs with AFM, FM, and FIM phases, seems to be extremely interesting to study how the magnetic response is modified when different magnetic couplings are

present. Such opportunity is given herein, where besides a conventional Fe/Fe-oxide core-shell configuration, a high percentage of $\gamma$-Fe was simultaneously formed.

Other authors have recently reported the formation of the face-centered cubic (FCC) crystalline phase ($\gamma$-Fe, the high-temperature stable phase for pure Fe) in diverse Fe-based nanostructured materials. Up to now, this $\gamma$-Fe phase was observed in small iron precipitates embedded in a Cu matrix,[38] in FeCu mechanically alloyed compounds,[39,40] in the synthesis of carbon nanotubes,[41–48] or in Fe-NPs and thin films but confined down to a few monolayers of thickness.[49–55] The magnetism of $\gamma$-Fe phase depends strongly on the Fe-Fe interatomic distances[56] although both the morphology of the sample and the particle size could play an important role. Indeed, AFM interactions are favored at low temperatures ($T < 100$ K) and for lattice parameters, $a < 3.6$ Å, while FM state with high Fe magnetic moment values ($\mu > 2.5\mu_B$) can be stabilized for $a > 3.6$ Å.[38,57] However, the simultaneous presence of $\alpha$-Fe and $\gamma$-Fe phases in a sample makes the study of $\gamma$-Fe phase difficult from both structural and magnetic points of view, and contradictory results have been published.[58] It was reported a low spin and AFM ordered state below 20 K in Fe-Ni alloys.[59,60] Some studies on FCC-Fe films found AFM response below 80 K (Ref. [53]) while others assured that magnetic ordering occurs at around 65 K.[61] On the contrary other exhaustive studies from $^{57}$Fe Mössbauer spectrometry on FCC-Fe particles show that they behave as paramagnets at least down to 1.8 K.[50] On the other hand, several studies on carbon nanotubes reveal that FCC-Fe NPs undergo an AFM transition around 80–100 K.[41,42] Therefore, the formation of considerable amount of $\gamma$-Fe phase in Fe-NP systems open new possibilities for the study of the striking magnetism of $\gamma$-Fe. The reason for the stabilization of the $\gamma$-Fe phase at room temperature is unclear. However, some authors have reported that the interstitial incorporation of carbon atoms in the FCC lattice could be the main reason for the appearance of $\gamma$-Fe.[51]

For those reasons, the combination of different experimental techniques is required for the complete understanding of the magnetic behavior of the $\gamma$-Fe phase. Herein, we have followed an easy chemical synthesis route, based on the *in situ* preparation of iron nanoparticles within the nanopores of an activated carbon. The NPs formed contain iron in both BCC and FCC crystal structures as well as Fe oxides. To investigate the microstructure, morphology, and magnetic properties of these Fe-NPs, several experimental techniques have been employed: scanning electron microscopy and transmission electron microscopy (SEM and TEM, respectively), x-ray diffraction (XRD), Fe $K$-edge x-ray absorption spectroscopy (XAS), $^{57}$Fe Mössbauer spectrometry, and magnetization measurements.

## II. SAMPLE PREPARATION AND EXPERIMENTAL DETAILS

The iron-carbon nanocomposites were synthesized using a commercial activated amorphous and porous carbon (M30) supplied by Osaka Gas (Japan) as the starting material. This activated carbon (AC) exhibits a large Brunauer-Emmett-Teller surface area (2350 m$^2$ g$^{-1}$), a high pore volume (1.47 cm$^3$ g$^{-1}$), and a porosity made up of mesopores with a size around 6–7 nm. The synthetic method consists of a pyrolysis process that takes place inside the restricted volume formed by the pores of the AC. The pores of the AC were filled with a solution of iron nitrate in ethanol up to the incipient wetness point and then dried at 350 K for 2 h. This process was repeated up to attain $\sim 17$ wt % Fe in the final composite. Subsequently, the composite was heat treated under N$_2$ up to 1173 K and maintained at this temperature for 3 h. The as-resulting product was cooled under nitrogen down to room temperature and then exposed to a small stream of air to stabilize it. This procedure allowed thus to successfully prepare the Fe-AC powered sample. The Fe content determined by thermogravimetric analysis, was 16.8 wt % Fe. The textural properties of the Fe-AC composite (determined by nitrogen physisorption, ASAP-2010) are $S_{BET}$ $\sim 750$ m$^2$ g$^{-1}$ and pore volume of 0.6 cm$^3$ g$^{-1}$. Further details of the preparation are given elsewhere.[11]

The morphology of the powdered sample was studied with a SEM JEOL JSM-6100. The particle-size distribution was estimated from TEM images obtained using a JEOL 2000-EXII operating at 180 kV. The specimens for the TEM analysis were prepared by dispersing a little amount of powder in ethanol.

Room temperature XRD pattern was collected on a high-resolution Seifert XRD 3000T diffractometer in Bragg-Brentano geometry using Cu $K\alpha$ radiation ($\lambda = 1.5418$ Å). A LaB$_6$ standard sample was used as calibration. The Rietveld refinement of the pattern has been performed using the FULL-PROF package and following the procedure developed by Martínez-Blanco *et al.*[62] for nanostructured systems.

XAS experiments were performed on the SPline beamline at the ESRF. Fe $K$-edge absorption spectra were recorded at room temperature in the transmission mode. For all spectra, a metallic Fe reference foil was used to provide an energy calibration for the monochromator. For the measurements, homogeneous layers of the powdered samples were made by spreading of fine powders of the material on an adhesive tape. Thickness and homogeneity of the samples were optimized to obtain the best signal-to-noise ratio. The absorption spectra were analyzed according to standard procedures[63] and the spectra were normalized to the averaged absorption coefficient at high energy in order to eliminate the dependence of the absorption on the sample thickness.

The Mössbauer spectra were recorded at 4.2, 77, and 300 K with a conventional constant acceleration spectrometer in transmission geometry using a $^{57}$Co/Rh source. The sample consists in a thin-powdered layer containing about 5 mg of Fe/cm$^2$. The experimental setup was calibrated using a standard $\alpha$-Fe foil while the values of isomer shift were quoted to that of $\alpha$-Fe at 300 K.

The temperature dependence of the magnetization, $M(T)$, was measured using a Quantum Design PPMS-14T magnetometer with the vibrating-sample magnetometer (VSM) option, and under nine applied magnetic fields $H = 10, 25, 50, 100, 250, 500, 1000, 5000, 10000$ Oe. First, the sample was cooled in zero field (ZFC) from 300 K down to 10 K, then a magnetic field, $H$, was applied and kept con-
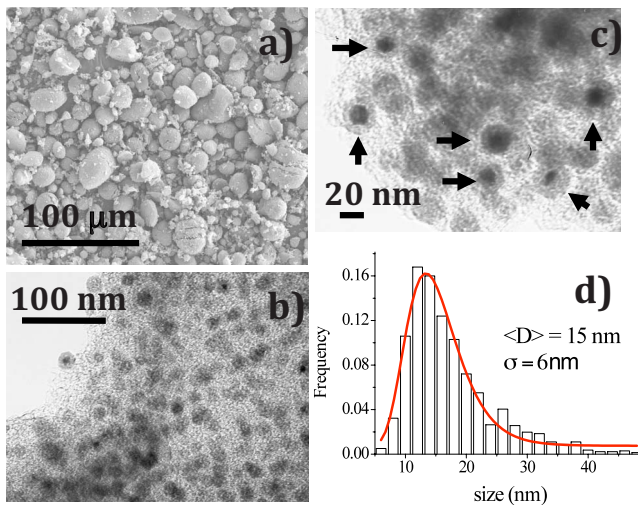
FIG. 1. (Color online) (a) SEM image showing almost spherical AC powders with a size in the 10–60 $\mu$m range. [(b) and (c)] Different details of TEM images for Fe-NPs. Arrows are pointing out Fe-NPs with different core/shell morphology. (d) Histogram of the NP diameter together with a fit (red solid line) to a log-normal function. The mean particle size obtained is $\langle\tau(\sigma)\rangle=15(6)$ nm.

stant. The magnetization, $M_{ZFC}$, and $M_{FC}$ were measured at fixed temperatures ($\Delta T=2$ K) between 10 and 340 K and 340 K down to 10 K, respectively. A commercial Oxford Instruments 1.2 T resistive VSM magnetometer equipped with a furnace was used to measure the magnetization vs temperature between 300 and 750 K under an applied magnetic field of 100 Oe. Magnetization vs applied magnetic field, $M(H)$ curves, were obtained using a superconducting quantum interference device magnetometer (Quantum Design) in the range $\pm20$ kOe ($M$ was measured under around 100 different values for $H$), and at selected temperatures between 10 and 350 K [hereafter denoted as $M(H)@ZFC$]. Additional $M(H)$ curves were collected at several fixed temperatures after cooling the sample from 350 K down to the selected temperature under an applied magnetic field ($H_{cool}$) of 20 kOe [henceforth designated as $M(H)@FC$].

## III. MORPHOLOGY, MICROSTRUCTURE, AND CRYSTALLINE STRUCTURE

### A. Electron microscopies: SEM and TEM

The AC powders are almost spherical in shape with a size in the 10–60 $\mu$m range as illustrated in the SEM image of Fig. 1(a). In order to obtain more information of the microstructure, the Fe-AC sample was observed by TEM [Figs. 1(b) and 1(c)]. The dark spots represent the metallic iron whereas the gray surface on the back is the porous carbon. The chemical synthesis route produces randomly dispersed NPs not always separated as distinguishable entities. After the evaluation of several TEM images, a histogram was generated from a large number of NPs ($>1500$) to model the particle size distribution [see Fig. 1(d)]. This analysis reveals that Fe-AC composite contains a unique and broad size distribution (5–50 nm) that is quite well described by a log-

normal distribution centered at $\langle\tau(\sigma)\rangle=15(6)$ nm. It is important to emphasize that Fe-NPs exhibit sizes larger than that of the pores of the carbon matrix ($\sim6$–7 nm) (see Sec. II). Thus, the only possibility is that Fe-cluster agglomerates inside the carbon matrix where several pores are interconnected. The arrows in Figs. 1(c) are pointing out Fe-NPs surrounded by a shell of $\sim4$–5 nm. The structural and chemical identification of this shell remains difficult because of the similar absorption contrast of the shell and the carbon host.

TEM images of Fe-AC sample also display that the carbon matrix can either be amorphous or exhibit a graphitic morphology due to the several processes that take place on the activated carbon filled with iron nitrate. The graphitic domains observed in the composites result from the catalytic phase conversion from amorphous carbon which occurs at temperatures $>1000$ K in the presence of Fe nanoparticles.[64–66] On heating the activated carbon filled with iron nitrate, iron oxides are formed around 473 K and, during the subsequent heating above 973 K the reduction in the iron oxides by means of the carbon ($Fe_xO_y+yC\rightarrow xFe+yCO$) leads to the formation of iron nanoparticles. The size of these metallic NPs grows as the temperature increases. The Fe-NPs catalyze the conversion of the surrounding amorphous carbon into the graphitic phase via the appearance of $Fe_xC_y$. As a result of this, for the composites prepared at high temperatures ($>1100$ K), the Fe-NPs grow up surrounded by the graphitic carbon nanostructures (i.e., nanocapsules). Indeed, in the case of Fe-AC sample, TEM images display both graphitelike and amorphouslike zones due to the final attained temperature (1173 K).

### B. X-ray diffraction

The room temperature XRD pattern for the Fe-AC sample is illustrated in Fig. 2. The main diffraction peaks of the diffraction profile were indexed as the Bragg reflections of BCC and FCC crystal structures with lattice parameter values of 2.867(1) and 3.587(1) Å, which unambiguously correspond to those of $\alpha$-Fe and $\gamma$-Fe phases, respectively. It should be noted that the most intense peaks [i.e., $\alpha$-Fe (110) and $\gamma$-Fe (111)] are quite close ($d\sim2$ Å). As the amorphous AC represents $\sim80$ wt % of the total mass of Fe-AC sample, the XRD pattern exhibits a large background contribution coming from the disordered amorphous matrix. In the literature, there is no general agreement as to what the real structure of this activated carbon is.[67] Therefore, the profile fit of the diffraction pattern of the Fe-AC composite, has to be performed considering amorphous "bumps" coming from this complex carbon matrix. This feature was also observed in previous works from other metallic AC composites.[7,8] Moreover, the size-strain peak broadening analysis[62] reveals that this broadening originates from size effects with a negligible strain. However, the large background intensity makes a precise estimation of the mean size of the nanoparticles difficult, although these values are below 40 nm, which is consistent with those obtained from TEM images. The relative percentage between $\alpha$-Fe and $\gamma$-Fe phases has been estimated to be around 50(10)%. This high relative percentage
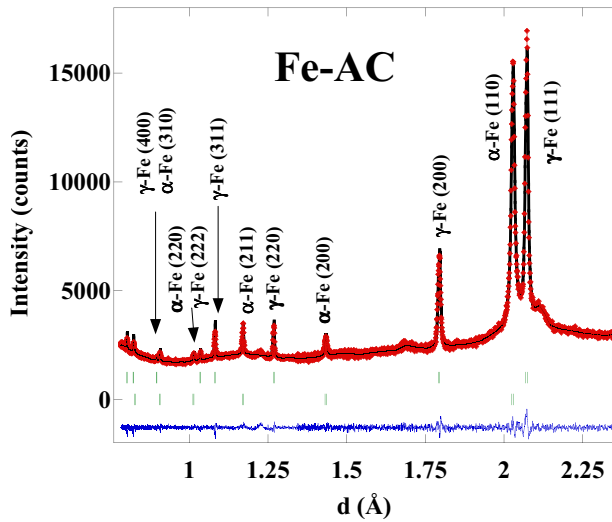
FIG. 2. (Color online) Observed (points) and calculated (solid line) room temperature powder XRD pattern for Fe-AC composite. First series of vertical bars correspond to the position of the Bragg reflections associated with the crystal structure of $\gamma$-Fe and the second one with that of $\alpha$-Fe. The observed-calculated difference pattern is depicted at the bottom of the figure.

of $\gamma$-Fe and the good signal vs noise relationship allow us an exhaustive study of this striking crystalline phase and stress the importance of the followed synthesis procedure among others that only provides small amounts of $\gamma$-Fe.[49]

It has been mentioned that the last step of the synthesis route (see Sec. II) consisted in exposing the sample to air in order to stabilize the Fe-NPs. Surprisingly, no significant traces of Fe oxides were observed in the XRD pattern, although due to the fast reactivity of iron in contact with oxygen, a thin layer of 2–3 nm is expected to cover the Fe-NPs in Fe-AC sample. However, the dimensions of that kind of layers do not exceed the minimum crystalline coherence length needed for diffraction to be clearly detected.[68] In addition, taking into account that around 80 wt % of the final composite is carbon, the content of Fe oxides, if any, would be below 5 wt % of the composite and so, beyond the limit of detection of XRD. Other complementary techniques should help in shedding light on this issue.

### C. $^{57}$Fe Mössbauer spectrometry

The $^{57}$Fe Mössbauer spectra recorded at 300 and 77 K are compared in Fig. 3. They mainly consist of a central single line and magnetic features. The analysis of the spectra confirms the presence of $\gamma$-Fe and $\alpha$-Fe phases and also the existence of an iron oxide phase. Hence, the transmission Mössbauer spectra were crucial to confirm that the Fe-NPs are oxidized as it was expected from the chemical preparation. The refined values of hyperfine fields ($B_{HF}$), quadrupole shift ($2\varepsilon$), isomer shift ($\delta$), and the linewidth ($\Gamma$) are listed in Table I as well as the relative area of each component, estimated from the absorption assuming the same values of recoil-free fraction.

The spectrum recorded at 300 K can be satisfactorily described with three different components: (i) a well-defined
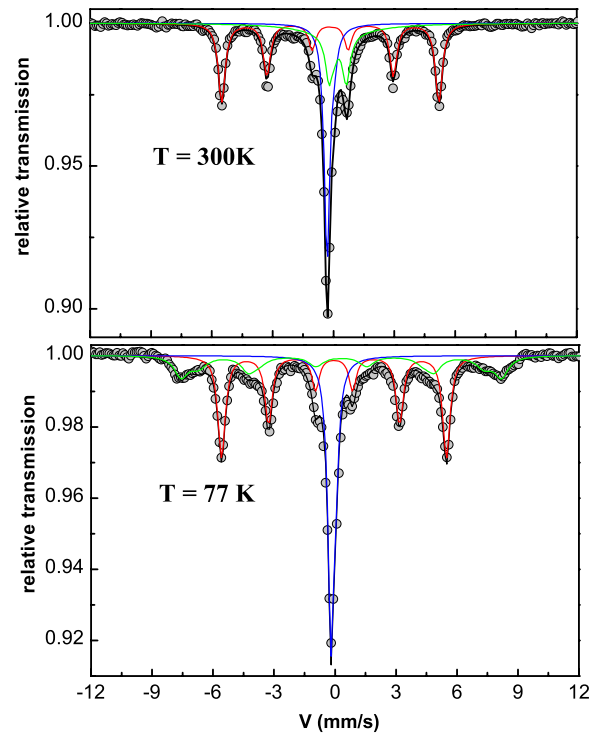


FIG. 3. (Color online) $^{57}$Fe Mössbauer spectra of the Fe NPs together with the fit obtained at 300 and 77 K. The black dots represent the experimental data and the solid lines the fitted spectra. Different subspectra corresponding to $\alpha$-Fe (red), $\gamma$-Fe (blue), and Fe-oxides (green) phases have been considered (see text for more details).

sextet with $B_{HF}(\approx 33.0$ T) attributed to the $\alpha$-Fe phase; (ii) an intense single peak with isomer shift ($\delta \sim -0.1$ mm s$^{-1}$) assigned to paramagnetic $\gamma$-Fe phase[44,45,53] (note that the value of the lattice parameter at room temperature, a $<3.6$ Å, suggests a nonferromagnetic state for $\gamma$-Fe), and (iii) a quadrupolar doublet plus a broad single line to better describe the baseline both with the same isomer shift ($\sim 0.38$ mm s$^{-1}$) typical of some ferric oxide species. The relative proportions are: 43(2)%, 28(2)%, and 29(1)%, respectively. Although no significant traces of Fe oxides were observed in the XRD profile (see above), the parameters obtained from the analysis of room-temperature Mössbauer spectrum reveal that the Fe-oxide species could be either magnetite ($Fe_3O_4$) or maghemite ($\gamma$-$Fe_2O_3$) but a mixture of both seems rather reasonable because of the oxidation of magnetite into maghemite.[69,70] Therefore, we expect FIM behavior as the $T_N$ of these oxides, in the bulk form, are 860 K ($Fe_3O_4$) and 1020 K ($\gamma$-$Fe_2O_3$). However, with respect to the Mössbauer time scale of $10^{-8}$ s, the quadrupolar structure of the Fe oxide displayed at room temperature unequivocally suggests the presence of superparamagnetic (SPM) fluctuations due to the existence of ultrafine domains while the broad single line does originate from domains the size of which is distributed and slightly larger.

On the other hand, the analysis of the Mössbauer spectrum at 77 K reveals that: (i) 45(2)% of the Fe atoms correspond the BCC Fe($B_{HF} \approx 34.1$ T); (ii) the $\gamma$-Fe is still present [$\sim 28(2)$%] with the same line width suggesting that

TABLE I. Parameters deduced from the analysis of the Mössbauer spectra depicted in Fig. 3. $B_{HF}$ is the hyperfine field; $\varepsilon$ and $\delta$ are the quadrupole splitting and isomer shift, respectively, with reference to an $\alpha$-Fe foil; $\Gamma$ is the line width (half width at half maximum). The proposed phase identification and their areas in relative percent are also given.

| $T$ (K) | Phase | $B_{HF}$ (T) | $\delta$ (mm/s) | $\varepsilon$ (mm/s) | $\Gamma$ (mm/s) | Area (%) |
|---|---|---|---|---|---|---|
| | $\alpha$-Fe | 33.0 | $\sim$0 | 0.01 | 0.21 | 43(2) |
| 300 | Fe oxides | | 0.38 | 0.75 | 0.22 | 14(1) |
| | | | 0.38 | | 2.0 | 15(1) |
| | $\gamma$-Fe | | −0.10 | | 0.18 | 28(2) |
| | $\alpha$-Fe | 34.1 | 0.12 | 0 | 0.22 | 45(2) |
| 77 | Fe oxides | 48.7 | 0.48 | 0.00 | 0.40 | 16(1) |
| | | 43.4 | 0.48 | 0.00 | 0.50 | 11(1) |
| | $\gamma$-Fe | | 0.02 | | 0.19 | 28(2) |

this FCC phase is stable even at 77 K and does not exhibit any magnetic ordering from 300 to 77 K. Besides that, two overlapping sextets related to the Fe-oxide species appear in the spectrum. Through this analysis it can be derived that the superficial oxides exhibit typical blocked magnetic order.

The hyperfine structure at 4.2 K (not shown in Fig. 3) is rather similar to that observed at 77 K, except for a slight increase in the line width of the singlet ($\Gamma \sim 0.22$ mm/s). Some authors ascribed such broadenings to low-temperature AFM transition.[41]

### D. X-ray absorption near-edge structure (XANES)

After confirming the existence of Fe oxides, only a technique selective to the atomic species, such as x-ray absorption spectroscopy, could provide precise information about the local atomic environment, and therefore, help to distinguish whether maghemite or magnetite is present in Fe-AC sample.[21] At the top of Fig. 4 the experimental Fe $K$-edge XANES spectrum of Fe-AC sample is shown together with those of $\alpha$-Fe, $\gamma$-Fe, $\gamma$-Fe$_2$O$_3$, and Fe$_3$O$_4$. The existence of Fe hydrooxides (goethite or ferrihydrite) was discarded by Mössbauer spectrometry. The experimental XANES spectrum of Fe-AC (red points in Fig. 4) was normalized at high energy after background subtraction to eliminate thickness dependence. In order to simulate the experimental data, we have performed a weighted sum (taking into account the phase percentages obtained from the fit of the Mössbauer data) of three XANES subspectra corresponding to $\alpha$-Fe foil, $\gamma$-Fe, and maghemite or magnetite. For the subspectra corresponding to the Fe oxides, data from Ref. 71 have been used while the Fe $K$-edge XANES subspectrum of a sample with FCC crystal structure and a lattice parameter of 3.592 Å (close to that obtained for the $\gamma$-Fe phase in Fe-AC sample, see above)[72] has been employed for $\gamma$-Fe. It can be observed in Fig. 4 that the simulated spectrum reproduces much better the shape, energy position of the different spectral features, their relative energy separation, and intensity ratio when maghemite is considered instead of magnetite. One cannot *a priori* exclude the occurrence of a disordered Fe oxide phase the structural and parameters of which are consistent with those observed in the present results.

### E. Nano-onion morphology

Considering that both BCC and FCC crystal structures are found for iron together with the presence of maghemite, the morphology of the Fe-NPs in Fe-AC sample can be explained as follows. Taking into account that, temperatures
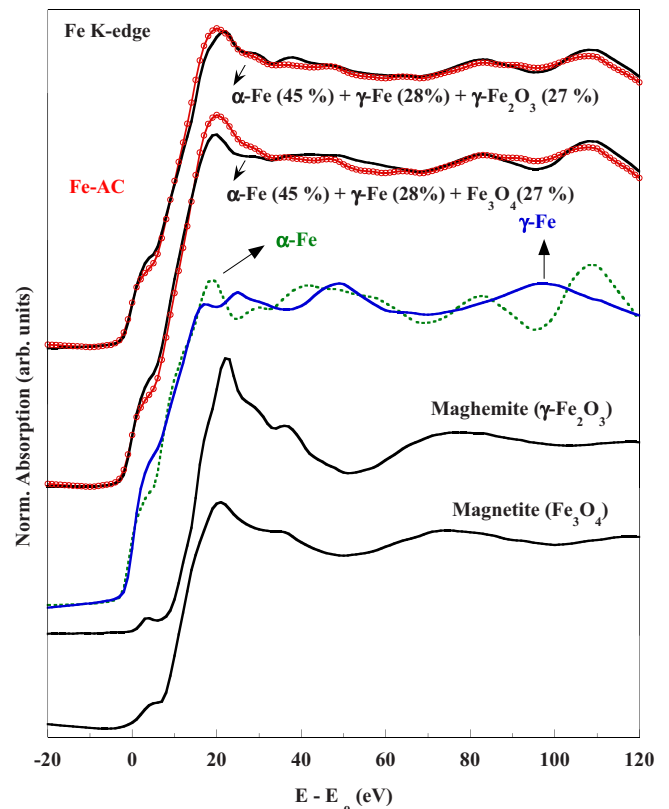


FIG. 4. (Color online) Fe $K$-edge XANES spectra for Fe-AC composite (red full circles) measured at room temperature together with the simulations (black lines). A mixture of $\alpha$-Fe (45%), $\gamma$-Fe (28%), and either $\gamma$-Fe$_2$O$_3$ or Fe$_3$O$_4$ (27%) has been used for the simulation. The spectra used to simulate the weighted sum (see text), $\alpha$-Fe foil (dotted line), Fe in FCC crystal structure, $\gamma$-Fe$_2$O$_3$, and Fe$_3$O$_4$ are also shown for clarity.

around that of the $\alpha$-$\gamma$ transition for pure iron (1183 K) are reached during the chemical synthesis route, we could assume that almost all Fe-NPs have FCC crystal structure at the highest temperature. However, the cooling process down to room temperature does not result in a complete transformation from FCC to BCC and the relative amount between both phases is maintained although the Fe-AC sample is cooled down to $T=4.2$ K (see Sec. III). Probably nitrogen and carbon impurities play a major role in the stabilization of a considerable amount of $\gamma$-Fe phase ($\approx 30\%$).[51] Hence, three possible morphologies can be proposed: (I) a mixture of core ($\alpha$-Fe)/shell ($\gamma$-Fe$_2$O$_3$) and core ($\gamma$-Fe)/shell ($\gamma$-Fe$_2$O$_3$) Fe-NPs; (II) a "nano-onion" core ($\gamma$-Fe)—double shell ($\alpha$-Fe/$\gamma$-Fe$_2$O$_3$) structure; or (III) a nano-onion core ($\alpha$-Fe)—double shell ($\gamma$-Fe/$\gamma$-Fe$_2$O$_3$) one. In order to elucidate what of these three possibilities is the most plausible, the magnetic measurements have been very relevant.

## IV. MAGNETIC BEHAVIOR

### A. Magnetization as a function of temperature

Figure 5 shows $M(T)$ curves measured under several applied magnetic fields, $H$, in both ZFC and FC regimes. Two important physical parameters can be obtained from these ZFC-FC data: (i) the temperature of irreversibility, $T_{irr}$, ($M_{ZFC}$ and $M_{FC}$ overlap for $T \geq T_{irr}$) and (ii) the blocking temperature, $T_B$, where the $M_{ZFC}(T)$ curves display a maximum. It is well established that $T_{irr}$ and $T_B$ are identical for an ideal SPM-like system of nanoparticles. In our particular study, $M_{ZFC}(T)$ measurements of Fe-AC sample exhibit a broad maximum around 170(40) K suggesting that there is a distribution of blocking temperatures rather than a unique and well-defined value for $T_B$. This means that a broad distribution of energy barriers exists, easily to understand if the distribution of NP sizes observed in TEM images [see Fig. 1(d)] is taken into account.

Moreover, $M_{ZFC}(T)$ and $M_{FC}(T)$ curves measured under $H < 500$ Oe, clearly show irreversibility in the whole temperature range, and this irreversibility persists up to 750 K as can be observed in the inset of Fig. 5. The latter indicates that the largest Fe-NPs remain blocked even up to 750 K, this temperature not being sufficiently high to overcome the energy barriers of the biggest Fe-NPs. For applied magnetic fields $H_{app} > 500$ Oe, the $M_{ZFC}(T)$ and $M_{FC}(T)$ curves overlap at $T_{irr} < 350$ K. The value of $T_{irr}$ exhibits a decreasing tendency as $H$ is raised ($T_{irr} \approx 50$ K for $H=10$ kOe, see Fig. 5).

In addition, $M_{ZFC}(T)$ recorded under $H < 500$ Oe exhibit a low-temperature "plateaulike" region that could be associated with the freezing of Fe-oxide magnetic moments, resulting in a spin-glasslike state. Furthermore, the saturating tendency of $M_{FC}(T)$ curve at low temperatures, when measured under low applied magnetic fields and, the upturns in $M_{FC}(T)$ measured under 5 and 10 kOe are also typical features for a canonical spin-glass system. Although at low temperatures the freezing of magnetic moments is assumed, a strong applied magnetic field forces their alignment to the field direction, thus giving rise to a progressive increase in $M_{FC}(T)$.
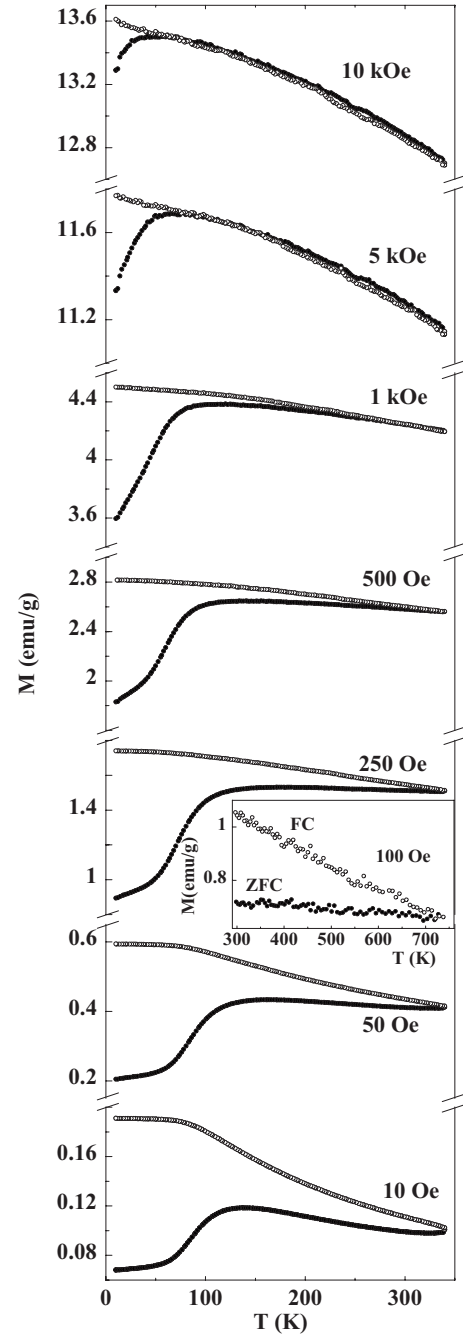


FIG. 5. $M(T)$ curve in the ZFC (full circles)—FC (open circles) regime under applied magnetic fields $H$ between 10 Oe and 10 kOe in the temperature range 10–340 K. Inset displays $M(T)$ ZFC-FC curve measured under 100 Oe between 300–750 K.

Furthermore, the lack of reversibility at low temperatures ($T < 50$ K), observed in $M_{ZFC}(T)$-$M_{FC}(T)$ curves measured under $H=10$ kOe, suggests that the spins are frozen in the field direction as the temperature is reduced. Since the anisotropy fields of $\alpha$-Fe and maghemite are small,[73] this $M(T)$ behavior is another consequence of the freezing state in the spin-glass shell below 50 K. Otherwise, the strong irreversibility typical of low-applied magnetic-field blocking process, should disappear on $M(T)$ above a few kOe.[13] This spin-glass state is expected on single thin coatings of ferrites
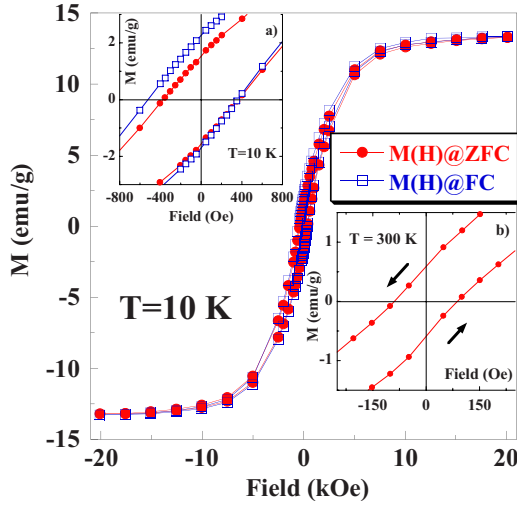
FIG. 6. (Color online) Hysteresis loops recorded at 10 K in ZFC (red full circles) and FC (blue open squares) regimes. Inset (a) displays an enlarged view of both $M(H)$@ZFC and $M(H)$@FC cycles at 10 K. Inset (b) shows in detail $M(H)$ cycle measured at 300 K.

at low temperature[74] but, attending to the possible double shell morphology (see Sec. III E), the scenario for these Fe-AC nanostructured powders is even more intricate. The spin-glasslike phase could exist at any of the interfacial regions between the Fe-oxide, $\alpha$-Fe, or $\gamma$-Fe phases. These interfaces and the surface inhomogeneities should undoubtedly modify the anisotropy and play a crucial role in modifying the values for the saturation magnetization, low-temperature coercive field and exchange-bias effect as it is discussed in the following section.

**B. Magnetization as a function of magnetic field**

The hysteresis loops, $M(H)$@ZFC and $M(H)$@FC for Fe-AC sample recorded at 10 K are displayed in Fig. 6 (see upper inset for an enlarged view around $M=0$). We will use $H_{right}$ and $H_{left}$ for the positive and negative magnetic field values, where the magnetization goes through zero in the hysteresis loops. Then, we define the exchange-bias field ($H_{ex}$) and the coercive field ($H_c$) as[27] $H_{ex}=-(H_{right}+H_{left})/2$ and $H_c=(H_{right}-H_{left})/2$. The existence of blocked NPs at room temperature is confirmed by the fact that $H_c(300 \text{ K}) \sim 100$ Oe and $M_r(300 \text{ K}) \sim 0.5$ emu/g (see lower inset in Fig. 6). In contrast, the low-temperature coercive field, $H_c(10 \text{ K})$, increases from 350 to 430 Oe after cooling the sample under an external magnetic field ($H_{cool}=20$ kOe). Left branches of $M(H)$@FC cycles are shifted to negative magnetic field values due to an EB effect. $H_{ex}$ value reaches 150 Oe at 5 K, it decreases monotonically with increasing temperature and eventually disappears around 50 K [see Fig. 7(a)]. This EB effect is observed when AFM (or FIM) and FM phases coexist, such as it occurs in Fe-AC sample, where coupling between $\alpha$-Fe with either $\gamma$-Fe and/or maghemite may be responsible for the appearance of a moderate exchange-bias effect.

**V. DISCUSSION**

Hysteresis loops show that the magnetization is not fully saturated even at 20 kOe (see Fig. 6), thus suggesting a non-
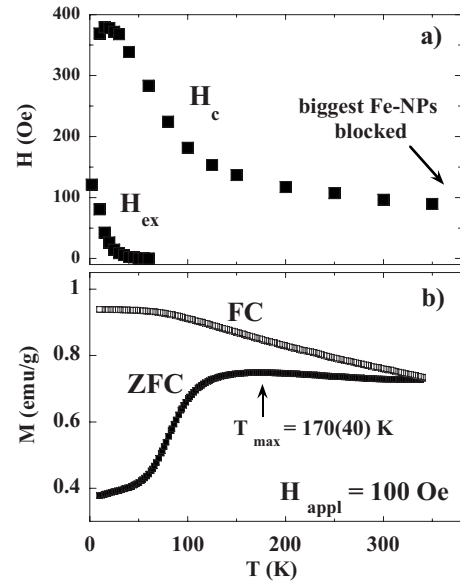


FIG. 7. (a) Temperature dependence of $H_{ex}$ and $H_c$ obtained from $M(H)$@FC and $M(H)$@ZFC hysteresis loops, respectively. (b) $M(T)$ ZFC-FC magnetization measurement under an applied magnetic field of 100 Oe in the temperature range 10–340 K. $M_{ZFC}(T)$ reaches a maximum value at $T_{max} \sim 170(40)$ K.

collinear arrangement of "intershell" magnetic moments.[19] Such effect could be related to random canting of magnetic moments or thermal disorder. This feature is also supported by the existence of a quadrupole doublet contribution, coming from the Fe oxide, to the room-temperature Mössbauer spectrum. However, the appearance of two sextets in the Mössbauer spectrum measured at 77 K associated with a maghemitelike oxide phase, confirms that the superparamagnetic thermal fluctuations of canted Fe-oxide magnetic moments disappear when the temperature is lowered, and the true ferrimagnetic nature of the oxide shell comes into view. Such a picture is consistent with: (i) $H_c(T)$ trend exhibits a maximum around 25 K [Fig. 7(a)]; (ii) $M_{ZFC}(T)$ and $M_{FC}(T)$ display a "plateaulike" behavior at low temperatures [Figs. 5 and 7(b)]; and (iii) high-field irreversibility between $M_{ZFC}(T)$ and $M_{FC}(T)$ below 50 K (Fig. 5).

The previous discussion would be the appropriate for $\alpha$-Fe NPs surrounded by FIM (or AFM) oxide shell or matrix.[19,75] However at the end of Sec. III E, it has been considered three possible morphologies for the Fe-AC nanoparticles: (I) a mixture of well-separated $\alpha$-Fe and $\gamma$-Fe cores with $\gamma$-Fe$_2$O$_3$-like shell; (II) a $\gamma$-Fe core—double ($\alpha$-Fe/$\gamma$-Fe$_2$O$_3$-like) shell, and (III) a $\alpha$-Fe core—double ($\gamma$-Fe/$\gamma$-Fe$_2$O$_3$) shell. One might consider that the concentration of impurities would be larger near the surface of the NPs, favoring thus the nano-onion morphology III. On the other hand, particles with different size may also have different impurity concentration in favor of model I. However, with the microstructures described by models I and III, leading to small dimensions of the $\alpha$-Fe cores, we should expect room temperature superparamagnetic behavior on magnetic measurements but this regime is not fully reached even at 750 K (see inset of Fig. 5). Consequently, attending to the magnetic response of Fe-AC sample, the most plausible
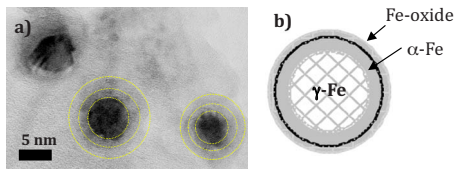
FIG. 8. (Color online) (a) TEM image showing in detail an Fe-NP with three different electronic densities and a well-defined "onionlike" morphology. In the figure, yellow lines are guides to the eye. (b) Schematic of the morphology of Fe-NPs in Fe-AC sample (see text).

nano-onion microstructure of the three above mentioned seems to be that of Fe-NPs with a $\gamma$-Fe core—double shell of $\alpha$-Fe/$\gamma$-Fe$_2$O$_3$ like.

With the aim of having an approximate value of the average width of each concentric shell, we assume that: (i) the NPs are spherical; (ii) the density is uniform; (iii) the average size of the Fe-NP is that obtained from TEM images [see Fig. 1(d)]; and (iv) the relative phase percentages are those calculated from Mössbauer and XANES spectroscopies. Then, a core ($\gamma$-Fe) of around 10 nm in diameter surrounded by a first shell ($\alpha$-Fe) of 1.9-nm thick and a thin outer shell ($\gamma$-Fe$_2$O$_3$) of 0.8-nm thick can be estimated. This morphology is schematically illustrated in Fig. 8(b). It is important to note that the mean thickness of the oxide layer is on the order of the lattice parameter, thus suggesting that both the morphology and the roughness could originate either ordered layer grown on the faceted $\alpha$-Fe shell or a disordered Fe-oxide phase in the case of rather spherical and rough $\alpha$-Fe shell. In addition, the reduced thickness of the Fe-oxide phase estimated around $\sim$1 nm, partially justify that although the presence of magnetite was discarded from the analysis of XANES, the values of the oxide phase parameters on the analysis of 77 K Mössbauer spectrum do not exactly correspond to those of a pure maghemite Fe-oxide phase (see Table I).

Considering this scenario, the exchange-bias coupling observed on $M(H)$@ FC cycles could be also produced by the coupling between the $\alpha$-Fe/$\gamma$-Fe phases. Mössbauer spectra reveal a slight increase in the line width of the singlet associated with $\gamma$-Fe, when cooling from 77 K down to 4 K (see Table I). Although a similar feature, observed by Prados *et al.*[41] on carbon nanotubes, leads them to the conclusion that an AFM transition appears at 100 K, no assumptions could be done for $\gamma$-Fe as its magnetic behavior is extremely dependent on the Fe-Fe interatomic distances, which are smaller ($a=3.587$ Å) than those stabilizing a ferromagnetic

coupling ($a>3.6$ Å). Indeed, the $\gamma$-Fe cores can be polarized by the $\alpha$-Fe shell and consequently, superparamagnetic fluctuations may be taken place for such small nuclei ($\sim$10 nm). It is worth noting that nano-onion morphology proposed is different respect to other nanoparticulate systems that found $\alpha$-Fe core surrounded by a shell of $\gamma$-Fe.[41,50]

On the other hand, the random dispersion of Fe-NPs through the carbon matrix makes them being close to each other or sometimes even into contact [see Figs. 1(c) and 8(a)]. As a result, magnetic interactions among particles may play an important role. Additionally, the existence of multidomain big particles could also be an important contribution. Consequently, these and other important issues such as the role played by a shell of $\gamma$-Fe require further investigations.

## VI. SUMMARY AND CONCLUDING REMARKS

Using a simple and easy to follow synthesis route, Fe nanoparticles have been deposited within the pores of an activated carbon. The resultant massive powder materials have been characterized combining different experimental techniques. The morphology of the Fe nanoparticles seems to be nano-onionlike formed by a $\gamma$-Fe nucleus surrounded by a concentric double shell of a $\alpha$-Fe and a thin outer shell of Fe oxide (maghemitelike). Only by combining both XANES and Mössbauer spectroscopies the relative percentage and nature of the different phases involved in the system have been precisely determined. At room temperature, the magnetic moments of the Fe oxide thermally fluctuate in a superparamagnetic state while a progressive freezing of these moments is found on cooling below 50 K. From all these findings, such description is partially supported by the magnetic exchange-bias coupling ($H_{ex} \approx 150$ Oe) of the ferrimagnetic Fe-oxide layer and the ferromagnetic $\alpha$-Fe. However, low-temperature antiferromagnetic transition of $\gamma$-Fe and its influence in the magnetic behavior of this nanostructured system could not be totally discarded.

---

*fernandezpaz.uo@uniovi.es

†pgorria@uniovi.es

‡jabr@uniovi.es

[1] X. Batlle and A. Labarta, J. Phys. D **35**, R15 (2002).

[2] S. Bedanta and W. Kleemann, J. Phys. D **42**, 013001 (2009).

[3] R. H. Kodama, J. Magn. Magn. Mater. **200**, 359 (1999).

[4] J. L. Dormann and D. Fiorani, *Magnetic Properties of Fine Particles* (North-Holland, Amsterdam, 1992).

[5] I. M. L. Billas, A. Châtelain, and W. A. de Heer, Science **265**, 1682 (1994).

[6] M. P. Fernández, D. S. Schmool, A. S. Silva, M. Sevilla, A. B. Fuertes, P. Gorria, and J. A. Blanco, J. Non-Cryst. Solids **354**,

5219 (2008).

[7] P. Gorria, M. P. Fernández-García, M. Sevilla, J. A. Blanco, and A. B. Fuertes, Phys. Status Solidi (RRL) **3**, 4 (2009).

[8] M. P. Fernández, D. S. Schmool, A. S. Silva, M. Sevilla, A. B. Fuertes, P. Gorria, and J. A. Blanco, J. Magn. Magn. Mater. (to be published).

[9] P. Gorria, M. Sevilla, J. A. Blanco, and A. B. Fuertes, Carbon **44**, 1954 (2006).

[10] A. B. Fuertes and P. Tartaj, Chem. Mater. **18**, 1675 (2006).

[11] M. Sevilla and A. B. Fuertes, Carbon **44**, 468 (2006).

[12] A. Slawska-Waniewska, M. Grafoute, and J. M. Greneche, J. Phys.: Condens. Mater. **18**, 2235 (2006).

[13] B. Martinez, X. Obradors, Ll. Balcells, A. Rouanet, and C. Monty, Phys. Rev. Lett. **80**, 181 (1998).

[14] D. L. Huber, Small **1**, 482 (2005).

[15] P. Tartaj, M. D. Morales, S. Veintemillas-Verdaguer, T. González-Carreño, and C. J. Serna, J. Phys. D **36**, R182 (2003).

[16] W. Andrä and H. Nowak, *Magnetism in Medicine: A Handbook* (Wiley, Berlin, 1998).

[17] L. T. Kuhn, A. Bojesen, L. Timmermann, M. M. Nielsen, and S. Mørup, J. Phys.: Condens. Matter **14**, 13551 (2002).

[18] C. M. Wang, D. R. Baer, J. E. Amonette, M. H. Engelhard, Y. Qiang, and J. Antony, Nanotechnology **18**, 255603 (2007).

[19] L. Del Bianco, D. Fiorani, A. M. Testa, E. Bonetti, L. Savini, and S. Signoretti, Phys. Rev. B **66**, 174418 (2002).

[20] D. Fiorani, L. del Bianco, A. M. Testa, and K. N. Trohidou, Phys. Rev. B **73**, 092403 (2006).

[21] L. Signorini, L. Pasquini, L. Savini, R. Carboni, F. Boscherini, E. Bonetti, A. Giglia, M. Pedio, N. Mahne, and S. Nannarone, Phys. Rev. B **68**, 195423 (2003).

[22] C. Baker, S. Ismat Shah, and S. K. Hasanain, J. Magn. Magn. Mater. **280**, 412 (2004).

[23] T. C. Rojas, J. C. Sánchez-López, J. M. Greneche, A. Conde, and A. Fernández, J. Mater. Sci. **39**, 4877 (2004).

[24] A. Slawska-Waniewska, A. Roig, M. Gich, Ll. Casas, K. Racka, N. Nedelko, and E. Molins, Phys. Rev. B **70**, 054412 (2004).

[25] A. Ceylan, C. C. Baker, S. K. Hasanain, and S. Ismat, J. Appl. Phys. **100**, 034301 (2006).

[26] J. Nogués, J. Sort, V. Langlais, V. Skumryev, S. Suriñach, J. S. Muñoz, and M. S. Baró, Phys. Rep. **422**, 65 (2005).

[27] O. Iglesias, X. Battle, and A. Labarta, J. Phys. D **41**, 134010 (2008).

[28] D. Fiorani, L. del Bianco, A. M. Testa, and K. N. Trohidou, J. Phys.: Condens. Matter **19**, 225007 (2007).

[29] V. Skumryev, S. Stoyanov, Y. Zhang, G. Hadjipanayis, D. Givord, and J. Nogués, Nature (London) **423**, 850 (2003).

[30] M. Kiwi, J. Magn. Magn. Mater. **234**, 584 (2001).

[31] J. Nogués and I. K. Schuller, J. Magn. Magn. Mater. **192**, 203 (1999).

[32] Q. K. Ong, A. Wei, and X.-M. Lin, Phys. Rev. B **80**, 134418 (2009).

[33] P. Miltenyi, M. Gierlings, J. Keller, B. Beschoten, G. Guntherodt, U. Nowak, and K. D. Usadel, Phys. Rev. Lett. **84**, 4224 (2000).

[34] U. Nowak, K. D. Usadel, J. Keller, P. Miltényi, B. Beschoten, and G. Güntherodt, Phys. Rev. B **66**, 014430 (2002).

[35] W. H. Meiklejohn and C. P. Bean, Phys. Rev. **102**, 1413 (1956).

[36] D. L. Peng, T. Hihara, K. Sumiyama, and H. Morikawa, J. Appl. Phys. **92**, 3075 (2002).

[37] L. Del Bianco, A. Hernando, M. Multigner, C. Prados, J. C.

Sánchez-López, A. Fernández, C. F. Conde, and A. Conde, J. Appl. Phys. **84**, 2189 (1998).

[38] S. H. Baker, A. M. Asaduzzaman, M. Roy, S. J. Gurman, C. Binns, J. A. Blackman, and Y. Xie, Phys. Rev. B **78**, 014422 (2008).

[39] P. Crespo, A. Hernando, R. Yavari, O. Drbohlav, A. G. Escorial, J. M. Barandiarán, and I. Orue, Phys. Rev. B **48**, 7134 (1993).

[40] P. Gorria, D. Martínez-Blanco, J. A. Blanco, M. J. Pérez, A. Hernando, L. F. Barquín, and R. I. Smith, Phys. Rev. B **72**, 014401 (2005).

[41] C. Prados, P. Crespo, J. M. González, A. Hernando, J. F. Marco, R. Gancedo, N. Grobert, M. Terrones, R. M. Walton, and H. W. Kroto, Phys. Rev. B **65**, 113405 (2002).

[42] A. Khasanov, J. He, J. Gaillard, K. Yang, A. M. Rao, C. M. Cameron, J. M. Schmeltzer, J. G. Stevens, and A. Nath, Appl. Phys. Lett. **93**, 013103 (2008).

[43] V. Pichot, P. Launois, M. Pinault, M. Mayne-L'Hermite, and C. Reynaud, Appl. Phys. Lett. **85**, 473 (2004).

[44] S. Groudeva-Zotova, R. Kozhuharova, D. Elefant, T. Mühl, C. M. Schneider, and I. Mönch, J. Magn. Magn. Mater. **306**, 40 (2006).

[45] T. Ruskov, I. Spirov, M. Ritschel, C. Müller, A. Leonhardt, and R. Ruskov, J. Appl. Phys. **100**, 084326 (2006).

[46] S. Karmakar, S. M. Sharma, M. D. Mukadam, S. M. Yusuf, and A. K. Sood, J. Appl. Phys. **97**, 054306 (2005).

[47] H. Kim and W. Sigmund, J. Cryst. Growth **276**, 594 (2005).

[48] C. P. Deck and K. Vecchio, Carbon **44**, 267 (2006).

[49] T. Enz, M. Winterer, B. Stahl, S. Bhattacharya, G. Miehe, K. Foster, C. Fasel, and H. Hahn, J. Appl. Phys. **99**, 044306 (2006).

[50] K. Haneda, Z. X. Zhou, A. H. Morrish, T. Majima, and T. Miyahara, Phys. Rev. B **46**, 13832 (1992).

[51] A. Kirilyuk, J. Giergiel, J. Shen, M. Straub, and J. Kirschner, Phys. Rev. B **54**, 1050 (1996).

[52] S. Tomita, M. Hikita, M. Fujii, S. Hayashi, and K. Yamamoto, Chem. Phys. Lett. **316**, 361 (2000).

[53] W. Keune, R. Halbauer, U. Gonser, J. Lauer, and D. L. Williamson, J. Appl. Phys. **48**, 2976 (1977).

[54] J. Thomassen, F. May, B. Feldmann, M. Wuttig, and H. Ibach, Phys. Rev. Lett. **69**, 3831 (1992).

[55] X. Sun, A. Gutierrez, M. J. Yacaman, X. Dong, and S. Jin, Mater. Sci. Eng., A **286**, 157 (2000).

[56] W. Pepperhoff and M. Acet, *Constitution and Magnetism of Iron and its Alloys* (Springer, Berlin, 2001).

[57] S. L. Palacios, R. Iglesias, D. Martínez-Blanco, P. Gorria, M. J. Perez, J. A. Blanco, A. Hernando, and K. Schwarz, Phys. Rev. B **72**, 172401 (2005).

[58] B. Wei, M. Shima, R. Pati, S. K. Nayak, D. J. Singh, R. Ma, Y. Li, Y. Bando, S. Nasu, and P. M. Ajayan, Small **2**, 804 (2006).

[59] D. G. Rancourt, S. Chehab, and G. Lamarche, J. Magn. Magn. Mater. **78**, 129 (1989).

[60] J. F. Valderruten, G. A. P. Alcázar, and J. M. Grenèche, J. Phys.: Condens. Matter **20**, 485204 (2008).

[61] W. A. A. Macedo and W. Keune, Phys. Rev. Lett. **61**, 475 (1988).

[62] D. Martinez-Blanco, P. Gorria, J. A. Blanco, M. J. Pérez, and J. J. Campo, J. Phys.: Condens. Matter **20**, 335213 (2008).

[63] D. E. Sayers and B. A. Bunker, *X-Ray Absorption: Principles, Applications, Techniques of EXAFS, SEXAFS, and XANES* (Wiley, New York, 1998), Chap. 6 and references therein.

[64] A. Ōya and H. Marsh, J. Mater. Sci. **17**, 309 (1982).

[65] H. Marsh, D. Crawford, and D. W. Taylor, Carbon **21**, 81 (1983).

[66] O. P. Krivoruchko and V. I. Zaikovskii, Kinet. Catal. **39**, 561 (1998).

[67] P. J. F. Harris, Z. Liu, and K. Suenaga, J. Phys.: Condens. Matter **20**, 362201 (2008).

[68] P. Tartaj, T. González-Carreño, O. Bomatí-Miguel, C. J. Serna, and P. Bonville, Phys. Rev. B **69**, 094401 (2004).

[69] T. J. Daou, S. Begin-Colin, J. M. Grenèche, F. Thomas, A. Derory, P. Bernhardt, P. Legaré, and G. Pourroy, Chem. Mater. **19**, 4494 (2007).

[70] T. J. Daou, J. M. Grenèche, G. Pourroy, S. Buathong, A. Derory, C. Ulhaq-Bouillet, B. Donnio, D. Guillon, and S. Begin-Colin, Chem. Mater. **20**, 5869 (2008).

[71] M. Wilke, F. Farges, P. E. Petit, G. E. Brown, and F. Martin, Am. Mineral. **86**, 714 (2001).

[72] P. Gorria, R. Boada, A. Fernández-Martínez, G. Garbarino, R. I. Smith, J. Chaboy, J. I. García Alonso, D. Martínez-Blanco, G. R. Castro, M. Mezouar, A. Hernando, and J. A. Blanco, Phys. Status Solidi (RRL) **3**, 115 (2009).

[73] R. K. Zheng, G. H. Wen, K. K. Fung, and X. X. Zhang, Phys. Rev. B **69**, 214431 (2004).

[74] R. H. Kodama, A. E. Berkowitz, E. J. McNiff, and S. Foner, Phys. Rev. Lett. **77**, 394 (1996).

[75] L. Del Bianco, D. Fiorani, A. M. Testa, E. Bonetti, and L. Signorini, Phys. Rev. B **70**, 052401 (2004).